

Fabrication And pH Sensing Characteristics Measurement of Back Gate ZnO Thin Film Planar FET

Ankita Porwal (✉ ankita.sporwal@gmail.com)

Malaviya National Institute of Technology <https://orcid.org/0000-0002-5219-5554>

Chitrakant Sahu

Malaviya National Institute of Technology

Research Article

Keywords: Zinc oxide, RF sputtering, pH sensing, Sensitivity

Posted Date: September 24th, 2021

DOI: <https://doi.org/10.21203/rs.3.rs-903030/v1>

License:  This work is licensed under a Creative Commons Attribution 4.0 International License.

[Read Full License](#)

Fabrication and pH Sensing Characteristics Measurement of Back Gate ZnO Thin Film Planar FET

Ankita Porwal · Chitrakant Sahu

Received: date / Accepted: date

Abstract Here in we demonstrate the design of a low-cost zinc oxide (ZnO) thin-film planar transistor-based pH sensor controlled by the bottom gate fabricated by a fairly simple fabrication approach. The performance of the fabricated device is evaluated by electrical as well as surface characterization. The surface morphology is analyzed by scanning electron microscope (SEM) and atomic force microscopy (AFM) and it shows surface properties that are essential for a device to function as a pH sensor. The fabricated thin-film FET comprises Zinc Oxide (ZnO) as a channel layer of length $6\ \mu\text{m}$ and thickness 200 nm, Silicon Nitride (Si_3N_4) as a passivation layer, and Aluminum (Al) as a contact layer. The effect on pH sensitivity for varied channel lengths ($6\ \mu\text{m}$, $12\ \mu\text{m}$, and $15\ \mu\text{m}$) is also examined and optimum results have been achieved at channel length = $6\ \mu\text{m}$. The change in threshold voltage (ΔV_{th}) & change in current (ΔI_{max}) are used as a sensing metrics to analyze the sensing performance of the device. The device shows excellent pH sensitivity in terms of average current and average voltage sensitivity 120.97 mA/pH and 97.85 mv/pH respectively at pH ranging from 3.2 to 11.1 with best pH stability (linearity) for pH value 4 to 10. The voltage sensitivity is higher than the Nernstian value (59 mv/pH) at room temperature.

Keywords Zinc oxide · RF sputtering · pH sensing · Sensitivity

Department of Electronics and Communication Engineering
Malaviya National Institute of Technology Jaipur Rajasthan-
302017, India
E-mail: ankita.sporwal@gmail.com

1 Introduction

The use of Field Effect Transistor (FET) in sensing devices permits particular interaction of sensitive elements and analytes that promotes label-free sensing. In 1970, Bergveld introduced Ion Sensitive Field Effect Transistor (ISFET) for pH sensing [1]. The device structure of ISFET is similar to MOSFET but the functioning of ISFET depends upon the reference electrode instead of a metal gate. For pH sensing mainly ISFET is used however, ISFET has some limitations such as low chemical stability, low isolation ability, and weak selectivity. To overcome the limitations of ISFET, Extended-Gate Field-Effect Transistor (EGFET) has been introduced by Van der Spiegel in 1983. EGFET has an advantage over ISFET in terms of easy manufacturing steps, low cost, insensitivity to light & temperature, high chemical & thermal stability, and stable electrical properties [2] but EGFET does not prefer as a miniaturized device because of the floating gate.

A biosensor is an analytical tool that translates biochemical reactions into a signal that can be measured. FET biosensor shows tremendous potential as a biomedical device and experiences a strong development in clinical application with high sensitivity. In comparison to other approaches, FET-based biosensors have a number of advantages, including great scalability, high sensitivity, low power consumption, and mass production at a reasonable cost [3]. Nanomaterial-based FET biosensors surpass traditional biosensors and promote high sensitivity. 2D nanomaterials are great candidates for FET biosensors because of their huge surface area, high carrier mobility, high mechanical strength, and flexibility [4].

pH sensors measure the concentration of hydrogen ions on a logarithmic scale and are used widely in clin-

ics, laboratories, and industries [5]. Recent developments in pH sensing technology demand a new material to replace conventional Silicon material and ZnO is an appropriate choice for this because of its physical and electronic properties. In comparison to Si, ZnO has higher mobility which is directly proportional to higher drain current and crystalline ZnO acquire at low temperature. ZnO is a transparent semiconductor with a high binding energy of exciton (60 meV) possessing piezoelectric, pyroelectric, and ferroelectric properties [6]. ZnO is nontoxic, biosafe with a high ionic bonding, insoluble at biological pH, and has a high isoelectric point (pI \sim 9.5) in comparison to other biomolecules hence easy immobilization of biomolecules [7]. ZnO is a compound wide bandgap (3.37 eV at room temperature) semiconductor from the group II-VI and it is crystalline in nature with a wurtzite (most stable) structure.

ZnO-based sensors already prove their effectiveness in the field of gas sensors, DNA detection, glucose detection, UV Photodetector, and pH detection [8]. In the literature, various methods have been proposed for the deposition of ZnO as a channel layer, for example, Chemical Bath Deposition (CBD), sol-gel technique, Chemical Vapor Deposition (CVD), sputtering, Molecular Beam Epitaxy (MBE), pulsed laser deposition, and inkjet printing, etc. [9, 10]. It is predicted that the proposed ZnO-based FET can replace silicon field-effect transistors as biosensors because of the high mobility of ZnO [11]. In the literature RF sputtering as a deposition technique is used for deposition of ZnO thin film and transparent ZnO TFT at room temperature, reported by many authors for various applications [12, 13].

The deposition method is an important factor in a sensor because it affects the crystallinity, microstructure, and homogeneity hence, to fabricate a biosensor, the sensing layer (ZnO layer) will be deposited by the RF sputtering method to get high-quality thin films using a patterned mask at room temperature. The benefits of the sputtering method include thickness control, repeatability of deposited films, high deposition rates, and large-scale uniformity. The sensing ability depends upon the functionalization layer and on the surface morphology. There is no external doping required in the ZnO layer and this layer will work as a sensing layer as well as the device layer hence being cost-effective. Doping in the ZnO resulted in defects that may affect the sensing behavior. The proposed structure also utilizes the advantage of the junctionless mechanism such as less fabrication complexity and low leakage current etc. [14]. In the crystal form of ZnO, zinc interstitials (Zn_i), and oxygen (O_v) vacancies are present which leads to n-type intrinsic ZnO [15]. Because of the

efficiency, reproducibility, and stability issue in p-type ZnO, fabrication of the device with p-type ZnO is not possible.

The main aim of this research is to fabricate a pH sensor with ZnO as a sensing layer. The fabricated device is tested for the concentration of hydrogen ion [H^+] represented in terms of pH value (acidic, neutral, and alkaline). There is a possibility that the pH solution affects the upper layer of the device so a thin passivation layer is required. A thin layer of Silicon Nitrate (Si_3N_4) is deposited as a passivation layer and it covers all areas including the source and drain except the gate and bond pad. The surface morphology of the ZnO layer was detected by SEM and AFM. For inline characterization, Dektak, Ellipsometer, and an optical microscope are used. The performance of a sensor is computed in terms of sensitivity as a figure of merit. Sensitivity is calculated in terms of change in threshold voltage (ΔV_{th}) and change in current (ΔI_{max}). This paper is organized in the following manner: Following the introduction, Section 2 discusses the simulation setup for the device, mathematical equivalent to pH value, mask design method, and fabrication process. Section 3 gives an overview of the structural & electrical characterizations and sensing behavior of the device. The important conclusions from the work are drawn in Section 4.

2 Device Design and Simulation

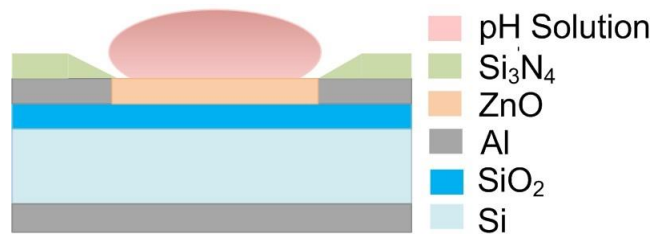


Fig. 1 Schematic structure of Back Gate ZnO Thin Film FET

Table 1 Set of parameters defined for ZnO during simulation of ZnO FET

Parameter Name	Symbol	Value	Unit
Electron mobility	μ_n	150	$cm^2V^{-1}s^{-1}$
Hole mobility	μ_p	30	$cm^2V^{-1}s^{-1}$
SRH lifetime of electrons	τ_n	4.2×10^{-6}	s
SRH lifetime of holes	τ_p	6.58×10^{-6}	s
Effective density of states in the conduction band	N_c	2.95×10^{18}	cm^{-3}
Effective density of states in the valance band	N_v	1.14×10^{19}	cm^{-3}
Electron affinity	χ	3.37	eV
Dielectric constant	ϵ	8.85	

Table 2 Concentration of ions and effective density of states in the conduction band and valence band at various pH

pH Concentration	The concentration of ions (mol/L)	Effective density of states in conduction band and valence band
3 (acidic)	$H^+ = 10^{-3}, OH^- = 10^{-11}$	$N_c = 2.33 \times 10^{-30}, N_v = 2.33 \times 10^{-22}$
5 (acidic)	$H^+ = 10^{-5}, OH^- = 10^{-9}$	$N_c = 2.33 \times 10^{-28}, N_v = 2.33 \times 10^{-24}$
7 (neutral)	$H^+ = OH^- = 10^{-7}$	$N_c = 2.33 \times 10^{-26}, N_v = 2.33 \times 10^{-26}$
8 (alkaline)	$H^+ = 10^{-8}, OH^- = 10^{-6}$	$N_c = 2.33 \times 10^{-25}, N_v = 2.33 \times 10^{-27}$
11 (alkaline)	$H^+ = 10^{-11}, OH^- = 10^{-3}$	$N_c = 2.33 \times 10^{-22}, N_v = 2.33 \times 10^{-30}$

The cross-sectional schematic structure of the back gate ZnO thin film FET is as shown in Fig. 1 and two-dimensional (2D) simulations of the proposed device have been carried out by the ATLAS TCAD simulator. In this device structure, a layer of SiO_2 of thickness 100 nm is thermally grown upon a 4-inch silicon wafer. A 200 nm thick layer of ZnO is sputtered on the oxide layer and to bring up the properties of ZnO during simulation, parameters shown in Table 1 are considered. The gate length is in the μm range ($6\mu m$, $12\mu m$, and $15\mu m$) according to fabrication constraints. For biasing,

a back gate of Aluminum with a thickness of 100 nm is taken. This device also considers n-channel junctionless structure in all regions (n-n-n type in source, channel, and drain region). The current conduction from source to drain region is controlled by back gate.

To precisely model, the device, a set of physical models are invoked for simulation including mobility

model, band model, Fermi-Dirac model, basic model, and Drift-Diffusion transport model. To accurately model the device, a defect statement is taken into account which considers the defect states present within the bandgap of ZnO. The mobility model is calculated in terms of electron and hole mobilities (μ_n and μ_p) of ZnO. Band model calculated the gain and radiative recombination in wurtzite material. The Fermi Energy model implemented a similar effect as Boltzmann statistics. The Drift-Diffusion model also accounts for radiative recombination. In addition to the following models, the basic model is also taken into account to model the device equivalent to the fabricated device. For the simulation of the device various equations (Poissons equation, continuity equation, and equations related to the drift-diffusion, energy valence & carrier transportation) are solved.

To model the pH, an ionic solution is considered an intrinsic semiconductor with a high dielectric constant ($k = 80$). The positive and negative ions in the solution are equivalent to electrons and holes in the semiconductor [16]. The properties of an ionic solution depend on the effective density of states in the conduction band and valence band (N_c and N_v). The dissociation of

H_2O is given as $H_2O = H^+ + OH^-$. At equilibrium law of mass action can be applied as

$$K_{eq} = \frac{[H^+][OH^-]}{H_2O} \quad (1)$$

The dissociation constant of water is given as

$$K_w = [H^+][OH^-] = 10^{-14} \quad (2)$$

Using Boltzmann statistics, electron and hole concentration is defined as

$$n = N_c \exp\left[\frac{E_F - E_c}{kT}\right], \quad p = N_v \exp\left[\frac{E_v - E_F}{kT}\right] \quad (3)$$

The mass action law of water ($n.p = n_i^2$) is also applicable to the intrinsic semiconductor. Assuming ($E_g = E_c - E_v$) above equation further simplifies in terms of effective density of states in the conduction band & valence and (N_c and N_v) given as

$$N_c = 2 \left[\frac{2\pi m_e kT}{h^2} \right]^{3/2}, \quad N_v = 2 \left[\frac{2\pi m_h kT}{h^2} \right]^{3/2} \quad (4)$$

Where m_e and m_h are the effective mass of electrons and holes respectively, h is Planck's constant (6.626×10^{-34} J.s), and k is the Boltzmann constant (1.38×10^{-23} J/K).

To calculate electrolyte equivalent semiconductor value of N_c and N_v , consider $[H^+] =$ Holes (p) and $[OH^-] =$ Electrons (n). Hence, for neutral solution at pH = 7, concentration of positive and negative ion is equal i.e. $[H^+] = [OH^-] = 10^{-7}$, therefore, effective density of states in conduction band and valence band will be equal i.e. $N_c = N_v = 2.33 \times 10^{-26} \text{ cm}^{-3}$. For acidic solution (pH < 7) concentration of positive ion decreases & negative ion concentration increases and effective density of states in conduction band depends upon negative ion concentration hence N_c value decreases and vice versa for N_v . For pH = 6, $[H^+] = 10^{-6}$ mol/L $[OH^-] = 10^{-8}$ mol/L. $[H^+]$, corresponding value of $N_c = 2.33 \times 10^{-27} \text{ cm}^{-3}$ $N_v = 2.33 \times 10^{-25} \text{ cm}^{-3}$. In alkaline solution (pH > 7) concentration of H^+ ions increases which relates the higher value of effective density of states in the valence band in comparison to effective density of states in conduction band. For pH =

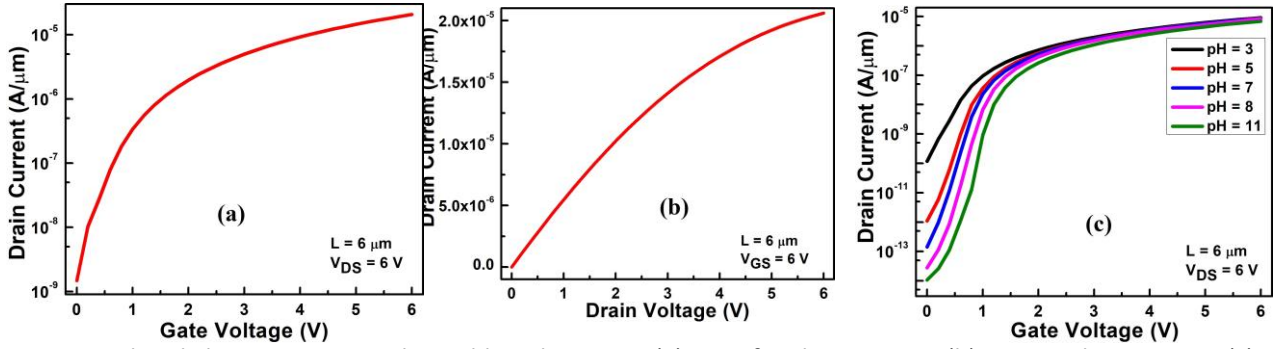
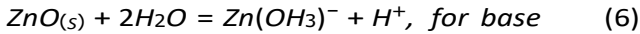


Fig. 2 Simulated characteristics at channel length = $6 \mu\text{m}$. (a) Transfer characteristic (b) Output characteristic (c) I_D Vs V_{GS} characteristics at different pH

8, $[H^+] = 10^{-8}$ mol/L and $[OH^-] = 10^{-6}$ mol/L, corresponding value of $N_c = 2.33 \times 10^{-25} \text{ cm}^{-3}$ and $N_v = 2.33 \times 10^{-27} \text{ cm}^{-3}$ [17]. The pH value at different concentration represented in terms effective density of states in conduction band and valence band as shown in Table 2.

The pH sensor is dependent on the surface mechanism. When pH solution interacts with sensing membrane (ZnO), ZnO surface is covered by the hydroxide group because of dissociation absorption of water. pH response depends upon the ion exchange in the surface layer containing (OH) groups. Protonation of the OH group occurs at lower pH which creates positive surface charge density at the surface while deprotonation occurs at higher pH resulting in negative surface charge density. The surface charge developed after interaction with pH solution can be expressed as:



As per the theory of site binding, the surface potential voltage between sensing membrane and pH solution can be given as [18,19]:

$$\psi = 2.303 \left(\frac{kT}{q} \right) \frac{\beta}{\beta+1} (pH_{pzc} - pH) \quad (7)$$

Where pH_{pzc} denotes the value at the point of zero charge, q represents the electron charge, k symbolizes the Boltzmann's constant, T is the absolute temperature, and β is the sensitivity parameter which can be calculated using [20].

$$\beta = \frac{2q^2 N_s \sqrt{\frac{K_a}{K_b}}}{kT C_{DL}} \quad (8)$$

Where N_s is the total number of the surface site per unit area, K_a and K_b represent acidic and alkaline constants respectively and C_{DL} is the double-layer capacitance.

The current characteristics obtained from the simulation setup are shown in Fig. 2. To calculate the drain current, the range of drain to source voltage (V_{DS}) and the gate to source voltage (V_{GS}) is varied from 0 V to 6 V. From I_D Vs V_{GS} characteristic as shown in Fig. 2(a), the device shows a high on current (2×10^{-5}) A/ μm at $V_{DS} = 6$ V. Fig. 2(b) indicates the output characteristic of the device at $V_{GS} = 6$ V. High on current relates the good driving capability and low off current denotes low leakage current. Initially, device characteristics are measured without consideration of pH and later with pH solution. Transfer characteristic of the device at different pH values (3, 5, 7, 8, and 11) is shown in Fig. 2(c) and pH values are calculated as shown in Table 2. Drain current is more for acidic concentration (pH = 3 & 5) and less in alkaline concentration (pH = 8 & 11) in comparison to a neutral concentration (pH = 7) because concentration of H^+ is more in acidic solution in comparison to alkaline solution.

2.1 Device Fabrication and Experimental Details

2.1.1 Mask Design

The proposed device measured the presence of hydrogen ions so the working of the device in different concentrations (acidic, neutral, and alkaline) is considered as shown in Fig. 3(a), and corresponding current characteristics are plotted in Fig. 3(b) at various pH solutions. The current characteristics are plotted for understanding the behavior of the device with change in pH solution and axes are not in exact scale value. In an acidic solution, H ions accumulate on the sensing surface with positive gate bias as shown in Fig. 3(a)

show higher current in comparison to neutral solution as shown in Fig. 3(b). Similarly, for the alkaline solution more OH^- ions are presently depicted by Fig. 3(a) (III). These OH^- ions lead to negative bias on the gate

so current decreases for alkaline solution represented in Fig. 3(b).

In a die of 8 mm X 8 mm, a total of 18 devices are arranged in 2 columns vertically as shown in Fig. 4(a). The sources of all devices are shorted together to form a common source point in this design, however, the drains of each device are extended by connecting wires, and the contact pad is 400 μm X 400 μm in size. There are two sources present in a single die where the source is represented by S, D_i shows the drain of the device, i denotes the device number & $i = (1, 2, 3... ,18)$. The enlarged view of a completely fabricated device is shown in Fig. 4(b)(III). Fig. 4(b) represents the optical microscopic top view of the device after lithography of layer-I (ZnO), layer-II (Al), and layer-III (Si_3N_4).

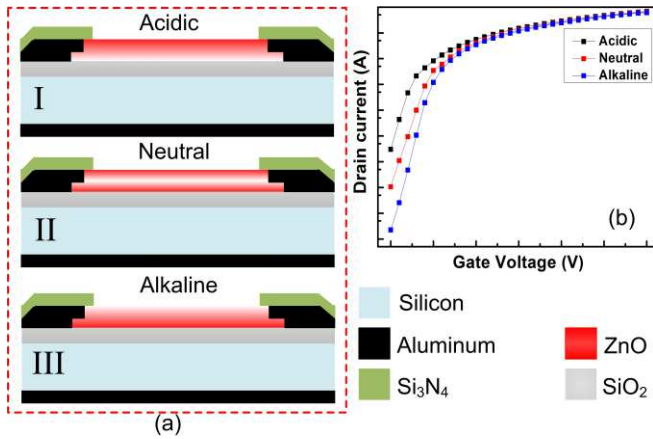


Fig. 3 (a) Working of the device in acidic, neutral, and alkaline solution (b) Corresponding current characteristics in different pH solution

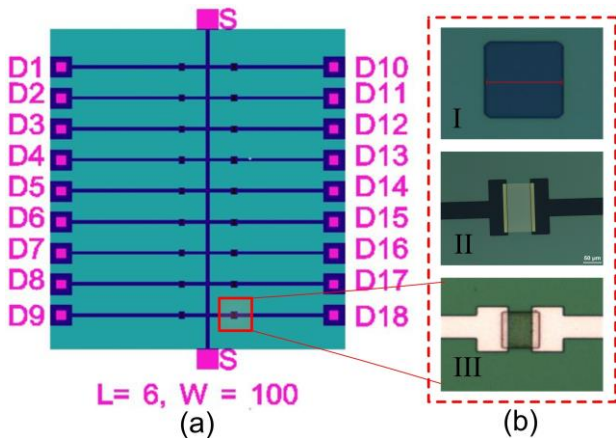


Fig. 4 (a) Mask design of a single die (b) Microscope images of the device after lithography of layer (I, II, and III)

2.1.2 Device Fabrication

Table 3 Dimensions of the different layers in the device

Name of the Layer	Length	Width	Thickness
SiO_2	Whole region	Whole region	100 nm
ZnO	6 μm	100 μm	200 nm
Aluminum (contacts)	400 μm	400 μm	400 nm
Al (back gate)	Whole region	Whole region	100 nm

The dimension of the different layers in the device is as shown in Table 3. The fabrication process started with the RCA cleaning of the silicon wafer of p-type, orientation $\langle 100 \rangle$ and, resistivity 1-10 Ω-cm. In RCA cleaning dip the wafer in a solution (a mixture of H_2O , NH_4OH , and H_2O_2 in the ratio of 5:1:1) and later in a mixture of H_2O , HCL, H_2O_2 in the ratio of 6:1:1 to remove the ionic contamination, organic and metal impurity. HF dip (DI water and HF in the ratio of 50:1) for 30 sec is given to remove the native oxide. The growth of silicon oxide (SiO_2) on one side of the silicon wafer is done by thermal oxidation. The SiO_2 thickness measured by the Ellipsometer is 98.8 nm and the refractive index value is 1.46. Optical Lithography of the first layer (i.e. ZnO layer) is performed by the MJB4 tool. Sample preparation for lithography: first clean the wafer with acetone, IPA, and DI water after that apply Hexamethyldisilazane (HMDS) as an adhesive layer, coat positive photoresist (PR) AZ5124E, and heat the sample at 110 °C for 1 minute. MF26A developer is used for the development of features of ZnO. ZnO deposition is done at the rate of 0.19 nm/sec by sputtering at room temperature. During deposition, the distance between substrate to target is 7.5 cm. 186.6 nm thickness and 1.96 is the refractive index of ZnO is measured by the Ellipsometer. Unwanted ZnO is removed by the lift-off process (dip the sample in acetone, IPA, and DI water for 2 hours).

Annealing of ZnO is carried out at 400 °C in an oxygen atmosphere. At the starting of the annealing process, nitrogen (N_2) and oxygen (O_2) will flow at the rate of 1 SLPM and 2 SLPM respectively and O_2 flow reduced to 1 SLPM at the end of the process. To perform lithography of the second layer i.e. aluminum layer, AZ5214E PR is coated on the sample at the speed of 4000 rpm for 40 seconds and soft bake at 110 °C for 1 minute. The deposition of Al as a contact layer is done by E-Beam evaporation in rotation mode and during this process chamber temperature is 35 °C. In the E-beam evaporator tool, the target to substrate distance is 35 cm the deposition rate is 5 A/S. Liftoff of Al is performed by immersing the sample in acetone, IPA, and DI water for 7 hours. The achieved thickness of aluminum is 438.55 nm measured by Dektak. In or-

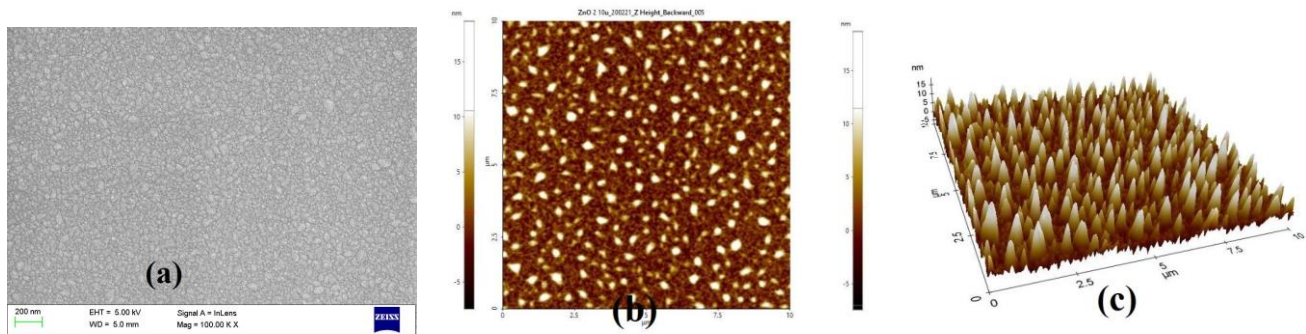


Fig. 5 (a) SEM image of ZnO blanket deposition on the substrate (b) 2 D image of ZnO surface after characterization by AFM (c) Three-dimensional AFM image of ZnO

der to prevent the deposition of the back gate on the front side, the wafer is coated (only the front side) with PR AZ5214E at the rate of 4000 rpm for 40 seconds and soft-back the sample at 110 °C for 1 minute. Al as back gate metal is deposited by sputtering at room temperature. The total deposition time is 420 sec, the deposition rate is 0.23 nm/s, and the chamber temperature is 23-27 °C during the process. The PR which is coated on the front side of the wafer before back gate deposition is removed by immersing the sample in acetone, IPA, and DI water for 3 min in each solution respectively. Silicon nitride (Si_3N_4) is deposited as a passivation layer by PECVD (Plasma Enhanced Chemical Vapor Deposition) method. The passivation layer is deposited in such a way that the sensing area will be uncovered. The process temperature is 350 °C, deposition time is 36 minutes and 142 nm/min is the deposition rate. Just before lithography of Si_3N_4 (passivation layer), coat PR AZ5214E on both sides of the wafer, and soft bake at 110 °C for 1 minute. To perform the etching of the Si_3N_4 layer, the sample size should be less than 4 inches to load in the dry etching tool. Aluminum nitride (AlN) is applied as an adhesive layer to the backside of the wafer and on the substrate holder. For the removal of undesired Si_3N_4 , dry etching is used. In the dry etching process, the temperature is 5 °C and SF_6 will flow for 40 seconds. Ashing is used for PR removal and O_2 will flow for 4 minutes in this process. The thickness of Si_3N_4 is 448.49 nm as measured by Dektak. Annealing of the Si_3N_4 layer is done at 450 °C in the nitrogen environment for 30 minutes in the dry oxidation tempress furnace tool. During the ramp-up and ramp-down, the flow rate of the nitrogen gas is 1 SLPM and during the process, N_2 flow rate is 3 SLPM. When the device fabrication is over, the dicing of the wafer is performed using automatic dicer DAD 32 into 8 mm X 8 mm dies.

3 Results and discussion

3.1 Structural characterization:

The sensing membrane is evaluated by Scanning Electron Microscope (SEM) and Atomic Force Microscopy (AFM). SEM requires an electrical contact on the surface so to make contact a thin layer (10 nm) of gold is deposited on the sample. SEM confirms that there are no pinholes or cracks generated on the ZnO surface as shown in Fig. 5(a) and measured average granular size 25 nm. The grown ZnO is aligned properly and has a uniform diameter. The morphology affects the number of binding site, which further impacts sensitivity.

The AFM images are shown in Fig. 5(b) and Fig. 5(c) represent the ZnO surface characterized by AFM in tapping mode and the measured RMS roughness is 2.9 nm over a scanning area of 10 μ m X 10 μ m. The small roughness value of 200 nm thick ZnO interprets the uniform surface of ZnO. From the 2-D image, the grain size is measured and from the 3-D image mean square roughness and roughness peak are calculated. These images confirm that good surface morphology of ZnO can be obtained by the RF sputtering method. The ZnO surface characterization shows a smooth surface with less roughness and film is uniformly distributed over the scan area. The uniform structure is directly proportional to the high surface-to-volume ratio of the sample which reflects the high crystallite size and increases the number of sites that are required for the ion exchange process [21].

3.2 Electrical Characterization:

The electrical characteristics are measured by the Agilent Probe Station. The fabricated device characteristics are shown in Fig. 6, 7, and 8 also represent good results, and pattern matches with the simulated results (Fig. 2). Prior to pH sensing, the electrical properties

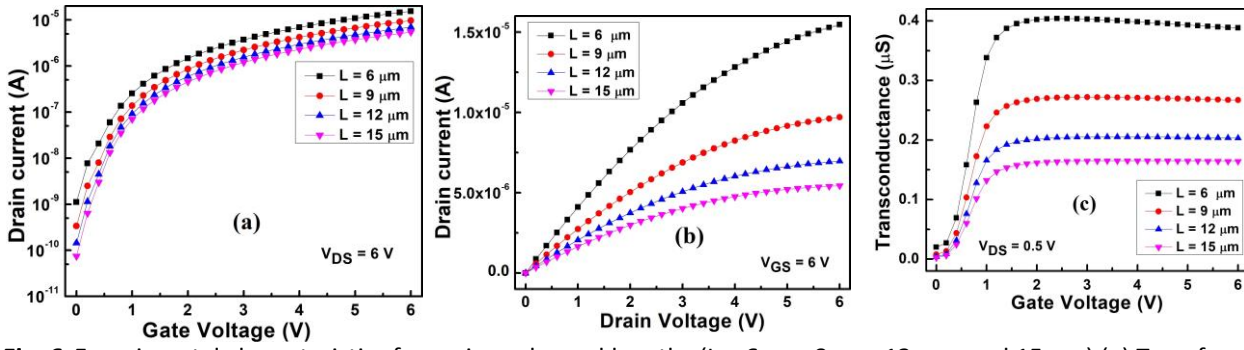


Fig. 6 Experimental characteristics for various channel lengths ($L = 6 \mu\text{m}$, $9 \mu\text{m}$, $12 \mu\text{m}$, and $15 \mu\text{m}$) (a) Transfer characteristics at $V_{DS} = 6\text{V}$ (b) Output characteristics at $V_{GS} = 6\text{V}$ (c) Transconductance curve

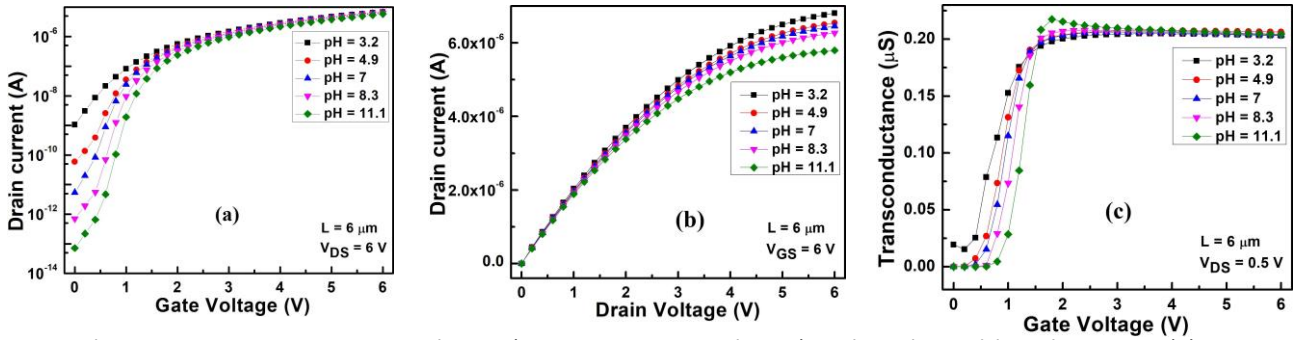


Fig. 7 Characteristics at various pH solution (3.2, 4.9, 7, 8.3, and 11.1) and at channel length = $6 \mu\text{m}$ (a) I_D Vs V_{GS} characteristics (b) I_D Vs V_{DS} characteristics (c) Transconductance at $V_{DS} = 0.5\text{V}$

of ZnO FET are assessed to examine connections between biosensor performance and the physical properties of the ZnO as depicts in Fig. 6 at various channel lengths ($L = 6 \mu\text{m}$, $9 \mu\text{m}$, $12 \mu\text{m}$, and $15 \mu\text{m}$). From the transfer characteristics as shown in Fig. 6(a), it can be concluded that the high on current is related to smaller channel length (L). The output characteristic is as shown in Fig. 6(b) also resembles that current is inversely proportional to the channel length. The transconductance curve as shown in Fig. 6(c) is plotted at drain voltage = 0.5V for different channel lengths and shows the highest transconductance value at $L = 6 \mu\text{m}$. The transconductance curve is sketched at low voltage ($V_{DS} = 0.5\text{V}$) to understand the working of the device in the subthreshold region.

To check the response of device for pH detection, different pH solution (Acidic = 3.2 and 4.9, Neutral = 7, and Alkaline = 8.3, and 11.1) is prepared by standard procedure and cross-verified by pH Meter. For testing the pH, pH solution is dropped cast on the sensing membrane with the help of the micropipette of precision $0.1 \mu\text{l}$. To prevent the sensor surface from corrosion after testing each solution, the device is cleaned with isopropyl alcohol (IPA).

The effect of pH concentration on the drain current and transconductance with respect to gate voltage is understood by curves shown in Fig. 7. At lower volt-

ages, current increases with the decrement in pH but at a higher voltage ($V_{DS} = 6\text{V}$ and $V_{GS} = 6\text{V}$) current is in the saturation region and shows less variation for pH can be seen from Fig. 7(a). Drain current is more for the acidic solution (pH = 3.2 and 4.9) and less for the alkaline solution (pH = 8.3 and 11.1) in comparison to neutral solution (pH = 7). In an acidic solution, accumulation of (H^+) ions occur at the surface and these ions attract the electrons towards the conducting channel hence lowering the resistance which leads to an increase in drain current. Similarly, alkaline solution (OH^-) accumulates at the surface hence lowering the threshold voltage and conductivity resulting in a decrement in the drain current. Output characteristics show the significant change in current with pH concentration at higher voltage represented in Fig. 7(b). The ratio of I_{ON}/I_{OFF} current increases (10^3 to 10^7) with the increases in pH (3.2 to 11.1) as estimated from Fig. 7(a). Transconductance at various pH is plotted at different gate voltages as shown in Fig. 7(c) and the transconductance pattern of the device is a little bit different at higher pH (11.1). The fabricated sensor shows rapid and favorable changes in pH concentration.

The functionality of the device is checked with different gate lengths at various pH solutions represented in Fig. 8. Transfer characteristics for gate length = $6 \mu\text{m}$, $12 \mu\text{m}$, and $15 \mu\text{m}$ at gate voltage from 0V to 6

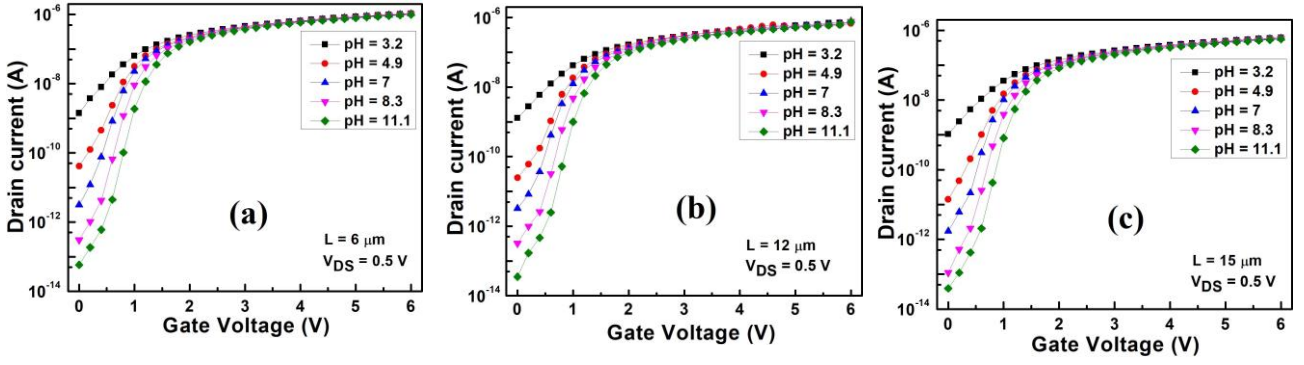


Fig. 8 Transfer characteristics at various channel lengths ($6 \mu\text{m}$, $12 \mu\text{m}$, & $15 \mu\text{m}$) and $V_{DS} = 0.5 \text{ V}$

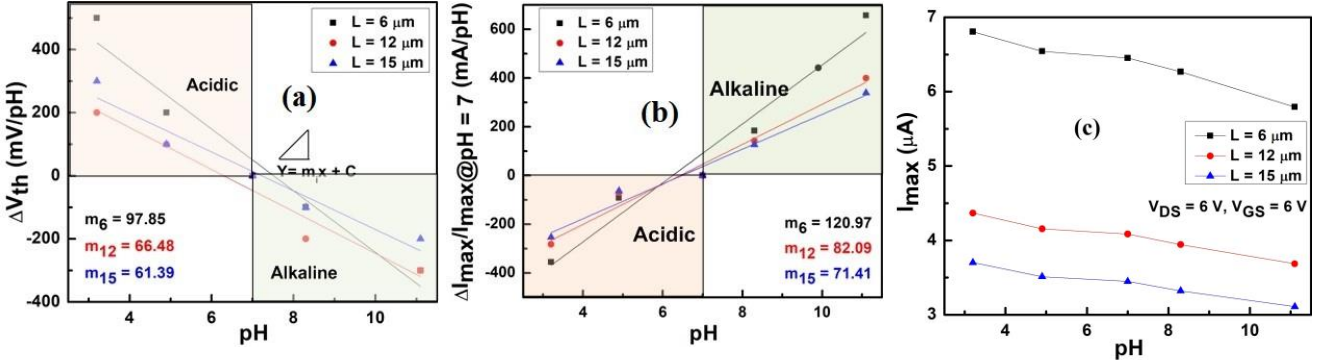


Fig. 9 At different pH concentrations (a) Sensitivity curve in terms of change in threshold voltage (b) Sensitivity curve in terms of change in maximum current (c) Maximum current

V are represented in Fig. 8(a), 8(b), and 8(c) respectively. At a first glance, current characteristics are looking almost similar for different gate lengths but I_{off} & I_{on} current changes with the channel length. At different pH, there is a major change in the current at the lower voltage but at higher voltage, the current shows minimal change with pH. The concentration of H^+ ion changes with the change in pH value hence current also changes. From Fig. 8 it can be concluded that with the increment in channel length, the current will decrease. With the reduction in channel length, the influence of source and drain on the channel increases similar to gate hence surface potential increases and this causes the increase in current. Drain current increases with the decrement in pH value which represents the n-type device behavior.

3.3 Sensing

The sensing capability of the device depends upon the fabrication process and material properties. To detect the presence of the hydrogen ion and analyze the sensitivity behavior of the device sensing metrics threshold voltage (ΔV_{th}) and change in current (ΔI_{max}) is used.

The average voltage sensitivity of the device is given by the equation, as follows:

$$Sensitivity = \frac{V_{th}(pH_1) - V_{th}(pH_2)}{pH_1 - pH_2} = \frac{\Delta V_{th}}{\Delta pH} \quad (9)$$

Similarly, The average current sensitivity of the device is calculated using the formula:

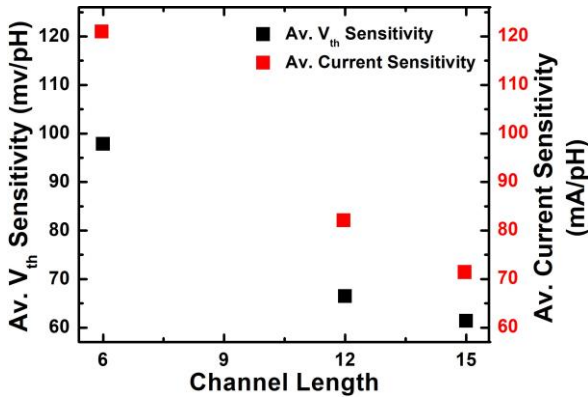
$$S = \frac{\Delta I_{max}}{I_{max@pH=7}} \quad (10)$$

The sensitivity is calculated in terms of threshold voltage (ΔV_{th}) and represented in Fig. 9(a) where symbols represent the measured data and solid line represents the linear fitted data. The sensitivity is calculated by linearly fitting of data where m represents the sensitivity (slope). In the pH range of 3.2 to 11.1, the device shows the highest sensitivity 97.85 mV/pH at $L = 6 \mu\text{m}$. With the increase in channel length voltage sensitivity decreases. Average current sensitivity is plotted in terms of $(\Delta I_{max}/I_{max@pH=7})$ as shown in Fig. 9(b) where sensitivity is calculated by linear fitting (solid line) of measured data (symbol). At gate length of $6 \mu\text{m}$, highest average current sensitivity i.e. 120.97 mA/pH is obtained in the pH range of 3.2 to 11.1 but at higher channel length ($L = 12 \mu\text{m}$ & $15 \mu\text{m}$) current sensitivity decreases. Hence, the channel length is an important parameter that affects the current sensitivity as well as

Table 4 Performance comparison with state of art devices.

Type of the device	Sensitivity ($\Delta V_{th}/V_{th}/pH$) (mv/pH)	pH range	Channel length (μm)
EGFET based pH sensor [22]	31.81	4-12	not reported
ZnO NR based sensor [23]	44.56	4-10	1.7
ZnO film-based sensor [23]	34.82	4-10	not reported
ZnO nanostructures [24]	48.2	4-12	not reported
ZnO nanowire-based EGFET pH sensor [25]	36.9	4-10	1
EGFET with unpassivated i-ZnO nanorod array [26]	44.01	4-12	0.08
EGFET with passivated i-ZnO nanorod array [26]	49.35	4-12	0.08
ZnO Thin Film FET [This work]	98.92	3.2-11.1	6
FDSOI based DG-ISFET [27]	379.2	3.3-10.6	10
DG SiNW FET [28]	720.7	4-10	20

voltage sensitivity. The maximum current for various channel lengths at different pH is drawn in Fig. 9(c) at $V_{DS} = V_{GS} = 6$ V. The current is higher for an acidic solution and lower for the alkaline solution in comparison to a neutral solution and the current decreases with the increase in pH & channel length. The above results indicate the good sensitive behavior of the fabricated device. All the measurements of the proposed device are performed at room temperature.

**Fig. 10** Average voltage and current sensitivity at various channel lengths

Theoretically, pH voltage sensitivity is measured at 59 mv/pH based on the Nernst equation at room temperature (300 K), also known as the Nernst limit [29, 30]. The fabricated sensor shows a higher voltage sensitivity (97.85 mv/pH) than the Nernst limit. Average threshold voltage and average current sensitivity at different channel lengths are plotted in Fig. 10 and show the highest average V_{th} sensitivity 97.85 mv/pH and average current sensitivity 120.97 mA/pH in the pH range of 3.2 to 11.1 at gate length of 6 μm .

In this graph (Fig. 10) black symbol denotes the average threshold voltage sensitivity and the red symbol denotes the average current sensitivity. Sensitivity depends on the channel length and it decreases with the

increase in the channel length. Average voltage sensitivity decreases (from 97.85 mv/pH to 66.48 mv/pH & 61.39 mv/pH) as channel length increases (from 6 μm to 12 μm & 15 μm) and similarly, average current sensitivity decreases (from 120.97 mA/pH to 82.09 mA/pH & 71.41 mA/pH) with the increase in channel length (from 6 μm to 12 μm & 15 μm). The performance of pH sensor also depends upon the surface-to-volume ratio and nanocrystallite size.

Performance comparison of the fabricated device is compared with the existing literature (ZnO-based pH sensor) as shown in Table 4. The proposed device shows excellent voltage sensitivity in comparison to existing literature. Prashant et al. fabricated EGFET based pH sensor and this device shows voltage sensitivity of 31.81 mv/pH in the pH range of 4 to 12. In comparison to ZnO film, ZnO NR-based pH sensor shows a higher voltage sensitivity because of the large surface to area volume ratio of ZnO nanowires and the total number of surface sites per unit area available for conduction as reported by S. J. Young et al. [23]. Aimi Bazilah et al. reported EGFET based pH sensor in which the sensing layer is fabricated by thermal chemical deposition (TCVD) method and calculated the sensitivity 48.2 mv/pH in the pH range of 4 to 12 [24]. Passivated ZnO film-based sensor and ZnO NR array have higher sensitivity than unpassivated devices because passivation reduces the Fermi level pinning effect [26]. Sensitivity depends upon the shape and size of ZnO nanostructure and it is extremely high when the device is operated in dual gate mode. From Table 4 it can be concluded that when the gate length is in the range of μm , sensitivity crosses the Nernst limit as reported by [27, 28].

4 Conclusion

Thin film planar FET structures have emerged as choicest devices for biosensing applications. The convenient

fabrication approach with uncompromised results have favored them to be the potential candidates for miniaturized biosensing techniques. We here report the simulation and fabrication of planar ZnO based thin film FET for pH detection. Herein the fabricated device is investigated by SEM & AFM and it shows a smooth homogeneous nanostructured surface. SEM calculated grain size of 25 nm and approved crystalline nature of ZnO. AFM determined RMS roughness of 2.9 nm over the scanning area of 10 μm X 10 μm . This device shows the potential to work as a pH sensor with excellent voltage sensitivity 97.85 mV/pH (higher than the Nernst limit) and average current sensitivity of 120.97 mA/pH at a channel length of 6 μm in the pH range of 3.2 to 11.1. The impact of pH on drain current for different channel lengths is also explored. The drain current decreases with the increase in pH because the presence of H^+ is more in the acidic solution in comparison to an alkaline solution. A smaller channel length is significant for a pH sensor because the highest sensitivity and drain current are obtained at a lower channel length. The sensing performance of the device with the pH solution is investigated by simulation and fabrication and it shows the most stable characteristics in pH range of 4 to 10. The simulated and fabricated results are in good agreement with each other.

5 Acknowledgment

Authors acknowledge the Centre for Nano Science and Engineering (CeNSE), Indian Institute of Science, Bengaluru for providing the fabrication and characterization facility under the Indian Nano Electronics Users Program (INUP).

Author's Contributions

This work was proposed and accomplished by Ankita Porwal (Author 1). Chitrakant Sahu supervised the entire work and made important discussions and modifications to the final manuscript.

Funding

The authors have not received any funding for this work.

Data Availability

There are no linked research data sets for this submission.

Conflict of interest

The authors declare that they have no conflict of interest.

Ethical Approval

All procedures performed in studies involving human participants were in accordance with the ethical standards of the institutional and/or national research committee and with the 1964 Helsinki declaration and its later amendments or comparable ethical standards.

Consent to participate

Informed consent was obtained from all individual participants included in the study.

Consent for publication

Not applicable

References

1. P. Bergveld, *Sensors and Actuators B: Chemical* **88**(1), 1 (2003). DOI [https://doi.org/10.1016/S0925-4005\(02\)00301-5](https://doi.org/10.1016/S0925-4005(02)00301-5)
2. S.A. Pullano, C.D. Critello, I. Mahbub, N.T. Tasneem, S. Shamsir, S.K. Islam, M. Greco, A.S. Fiorillo, *Sensors* **18**(11) (2018). DOI 10.3390/s18114042. URL <https://www.mdpi.com/1424-8220/18/11/4042>
3. M. Sedki, Y. Shen, A. Mulchandani, *Biosensors and Bioelectronics* **176**, 112941 (2021). DOI <https://doi.org/10.1016/j.bios.2020.112941>
4. N. Shafi, C. Sahu, C. Periasamy, *IEEE Electron Device Letters* **40**(6), 997 (2019). DOI 10.1109/LED.2019.2911334
5. J.H. Yoon, S.B. Hong, S.O. Yun, S.J. Lee, T.J. Lee, K.G. Lee, B.G. Choi, *Journal of Colloid and Interface Science* **490**, 53 (2017). DOI <https://doi.org/10.1016/j.jcis.2016.11.033>
6. D. Look, *Materials Science and Engineering: B* **80**(1), 383 (2001). DOI [https://doi.org/10.1016/S0921-5107\(00\)00604-8](https://doi.org/10.1016/S0921-5107(00)00604-8)
7. m. zgr, D. Hofstetter, H. Morko, *Proceedings of the IEEE* **98**(7), 1255 (2010). DOI 10.1109/JPROC.2010.2044550
8. Y. Zhang, M.K. Ram, E.K. Stefanakos, D.Y. Goswami, *Journal of Nanomaterials* **2012**, 624520 (2012). DOI 10.1155/2012/624520. URL <https://doi.org/10.1155/2012/624520>
9. Y. Fu, J. Luo, X. Du, A. Flewitt, Y. Li, G. Markx, A. Walton, W. Milne, *Sensors and Actuators B: Chemical* **143**(2), 606 (2010). DOI <https://doi.org/10.1016/j.snb.2009.10.010>
10. I. Ishteyaq, K. Muzaffar, *Superlattices and Microstructures* **145**, 106604 (2020). DOI <https://doi.org/10.1016/j.spmi.2020.106604>

11. H.S. Bae, S. Im, *Journal of Vacuum Science & Technology B: Microelectronics and Nanometer Structures Processing, Measurement, and Phenomena* **22**(3), 1191 (2004). DOI 10.1116/1.1756166. URL <https://avs.scitation.org/doi/abs/10.1116/1.1756166>
12. H.S. Bae, M.H. Yoon, J.H. Kim, S. Im, *Applied Physics Letters* **83**(25), 5313 (2003). DOI 10.1063/1.1633676. URL <https://doi.org/10.1063/1.1633676>
13. P.F. Carcia, R.S. McLean, M.H. Reilly, G. Nunes, *Applied Physics Letters* **82**(7), 1117 (2003). DOI 10.1063/1.1553997. URL <https://doi.org/10.1063/1.1553997>
14. J. Colinge, C. Lee, N.D. Akhavan, R. Yan, I. Ferain, P. Razavi, A. Kranti, R. Yu, in *Semiconductor-On-Insulator Materials for Nanoelectronics Applications* (Springer, 2011), pp. 187–200. DOI 10.1007/978-3-642-15868-1-10. URL <https://doi.org/10.1007/978-3-642-15868-1-10>
15. N.R. Shanmugam, S. Muthukumar, S. Prasad, *Future Science OA* **3**(4), FSO196 (2017). DOI 10.4155/fsoa-2017-0006. URL <https://doi.org/10.4155/fsoa-2017-0006>. PMID: 29134112
16. F. Pittino, P. Palestri, P. Scarbolo, D. Esseni, L. Selmi, *Solid-State Electronics* **98**, 63 (2014). DOI <https://doi.org/10.1016/j.sse.2014.04.011>. Selected Papers from ULIS 2013 Conference
17. R. Narang, M. Saxena, M. Gupta, *IEEE Transactions on Electron Devices* **64**(4), 1742 (2017). DOI 10.1109/TED.2017.2668520
18. R. van Hal, J. Eijkel, P. Bergveld, *Sensors and Actuators B: Chemical* **24**(1), 201 (1995). DOI [https://doi.org/10.1016/0925-4005\(95\)85043-0](https://doi.org/10.1016/0925-4005(95)85043-0)
19. D.E. Yates, S. Levine, T.W. Healy, *Journal of the Chemical Society, Faraday Transactions 1: Physical Chemistry in Condensed Phases* **70**(0), 1807 (1974). DOI 10.1039/f19747001807. URL <https://doi.org/10.1039/f19747001807>
20. T.M. Pan, M.D. Huang, C.W. Lin, M.H. Wu, *Sensors and Actuators B: Chemical* **144**(1), 139 (2010). DOI <https://doi.org/10.1016/j.snb.2009.10.049>
21. F.A. Sabah, N.M. Ahmed, Z. Hassan, M.A. Almessiere, *Materials Science in Semiconductor Processing* **71**, 217 (2017). DOI <https://doi.org/10.1016/j.mssp.2017.07.001>
22. P. Sharma, V.S. Bhati, M. Kumar, R. Sharma, R. Mukhiya, K. Awasthi, M. Kumar, *Applied Physics A* **126**(4), 284 (2020). DOI 10.1007/s00339-020-03466-w. URL <https://doi.org/10.1007/s00339-020-03466-w>
23. S.J. Young, L.T. Lai, W.L. Tang, *IEEE Sensors Journal* **19**(23), 10972 (2019). DOI 10.1109/jsen.2019.2932627. URL <https://doi.org/10.1109>
24. A. Bazilah, Z. Awang, S.S. Shariffudin, S.H. Herman, *International Journal of Engineering & Technology* **7**(3.11), 6 (2018). DOI 10.14419/ijet.v7i3.11.15919. URL <https://doi.org/10.14419>
25. S.P. Chang, C.W. Li, K.J. Chen, S.J. Chang, C.L. Hsu, T.J. Hsueh, H.T. Hsueh, *Science of Advanced Materials* **4**(11), 1174 (2012). DOI doi:10.1166/sam.2012.1410
26. Y.S. Chiu, C.Y. Tseng, C.T. Lee, *IEEE Sensors Journal* **12**(5), 930 (2012). DOI 10.1109/jsen.2011.2162317. URL <https://doi.org/10.1109/jsen.2011.2162317>
27. H.J. Jang, W.J. Cho, *Applied Physics Letters* **100**(7), 073701 (2012). DOI 10.1063/1.3685497. URL <https://doi.org/10.1063/1.3685497>
28. K. Zhou, Z. Zhao, P. Yu, Z. Wang, *Sensors and Actuators B: Chemical* **320**, 128403 (2020). DOI <https://doi.org/10.1016/j.snb.2020.128403>
29. A. Das, D.H. Ko, C.H. Chen, L.B. Chang, C.S. Lai, F.C. Chu, L. Chow, R.M. Lin, *Sensors and Actuators B: Chemical* **205**, 199 (2014). DOI <https://doi.org/10.1016/j.snb.2014.08.057>
30. O. Knopfmacher, A. Tarasov, W. Fu, M. Wipf, B. Niesen, M. Calame, C. Schenberger, *Nano Letters* **10**(6), 2268 (2010). DOI 10.1021/nl100892y. URL <https://doi.org/10.1021/nl100892y>